Chinese Chemical Letters 37 (2026) 110752

Contents lists available at ScienceDirect

Chinese Chemical Letters

journal homepage: www.elsevier.com/locate/cclet

The construction of $InVO_4/BiVO_4$ heterojunction *via* cation-exchange for efficient and highly selective CO_2 photoreduction to methanol

Cheng-Cheng Jiao[1], Guang-Xing Dong[1], Ke Su*, You-Xiang Feng, Min Zhang*, Tong-Bu Lu

MOE International Joint Laboratory of Materials Microstructure, Institute for New Energy Materials and Low Carbon Technologies, School of Materials Science and Engineering, School of Chemistry and Chemical Engineering, Tianjin University of Technology, Tianjin 300384, China

ARTICLE INFO

Article history:
Received 12 November 2024
Revised 1 December 2024
Accepted 11 December 2024
Available online 12 December 2024

Keywords:
Cation exchange
Charge transfer
CO_2 reduction
Heterojunction
Photocatalysis

ABSTRACT

Converting CO_2 into methanol (CH_3OH), a high-value-added liquid-phase product, through efficient and highly selective photocatalysis remains a significant challenge. Herein, we present a straightforward cation exchange strategy for the *in-situ* growth of $BiVO_4$ on an $InVO_4$ substrate to generate a Z-scheme heterojunction of $InVO_4/BiVO_4$. This *in-situ* partial transformation approach endows the $InVO_4/BiVO_4$ heterojunction with a tightly connected interface, resulting in a significant improvement in charge separation efficiency between $InVO_4$ and $BiVO_4$. Moreover, the construction of the heterojunction reduces the formation energy barrier of the *COOH intermediate during the photoreduction of CO_2 and increases the desorption energy barrier of the *CO intermediate, facilitating the deep reduction of *CO. Consequently, the $InVO_4/BiVO_4$ heterojunction is capable of photocatalytic CO_2 reduction to CH_3OH with high efficiency and selectivity. Under conditions where water serves as the electron source and a light intensity of 100 mW/cm^2, the yield of CH_3OH reaches 130.5 μmol g^{-1} h^{-1} with a selectivity of 92%, outperforming photocatalysts reported under similar conditions.

© 2025 Published by Elsevier B.V. on behalf of Chinese Chemical Society and Institute of Materia Medica, Chinese Academy of Medical Sciences.

The rapid advancement of global industrial modernization has led to excessive consumption of fossil fuels, causing a sustained and substantial rise in carbon emissions and subsequent detrimental environmental and climatic consequences [1–4]. To effectively mitigate the intensifying greenhouse effect, there is a global consensus on actively pursuing a green and low-carbon transformation of economy and society to achieve "carbon peaking and carbon neutrality" [5,6]. In recent years, photocatalytic CO_2 conversion technology has emerged as a promising approach, providing robust support for the realization of "dual carbon" goals [7–12]. Among various photocatalytic CO_2 reduction products, liquid-phase products stand out due to their high energy density and convenience in separation, storage, and transportation. Notably, methanol (CH_3OH), as a crucial chemical raw material and alternative energy source, holds a pivotal position in industrial production. Thus, leveraging semiconductor catalysts to convert CO_2 into CH_3OH through photocatalytic method not only addresses environmental challenges but also alleviates the energy crisis, making it a mutually beneficial strategy [13–18]. However, the process of photocatalytic CO_2 reduction to CH_3OH is complex, involving multiple charge transfers and extended reaction pathways, which leads to a higher rate of photogenerated charge recombination compared to their utilization in the reaction. This limits the catalytic activity and selectivity for CO_2 to CH_3OH conversion [19–25].

In recent years, metal vanadates, such as $BiVO_4$, $InVO_4$, and $FeVO_4$, have garnered considerable attention in photocatalysis due to their exceptional visible light absorption and robust stability [26–29]. Among them, $InVO_4$, with its suitable energy band structure, stands out as a promising catalyst for photocatalytic CO_2 reduction [30,31]. Moreover, it has been proven to achieve high selectivity for CH_3OH production [32]; $BiVO_4$ excels in photocatalytic water oxidation, attributed to its relatively high oxidation potential [33–35]. However, both $InVO_4$ and $BiVO_4$ suffer from limited photocatalytic activity due to insufficient carrier separation. Integrating $InVO_4$ and $BiVO_4$ into a Z-scheme heterojunction through methods, such as hydrothermal [36], dipping-calcination [37] and one-pot microwave [38], can enhance the separation efficiency of photogenerated carriers, leveraging their respective strengths in CO_2 reduction and water oxidation. Nevertheless, traditional methods often result in loose heterojunctions interfaces, limiting carrier separation efficiency. We herein propose a cation exchange strategy, involving the introduction of Bi^{3+} ions onto an $InVO_4$ substrate for *in-situ* conversion to $BiVO_4$, successfully constructing a direct

* Corresponding authors.
E-mail addresses: ksu2021@stud.tjut.edu.cn (K. Su), zm2016@email.tjut.edu.cn (M. Zhang).
[1] These authors contributed equally to this work.

https://doi.org/10.1016/j.cclet.2024.110752
1001-8417/© 2025 Published by Elsevier B.V. on behalf of Chinese Chemical Society and Institute of Materia Medica, Chinese Academy of Medical Sciences.

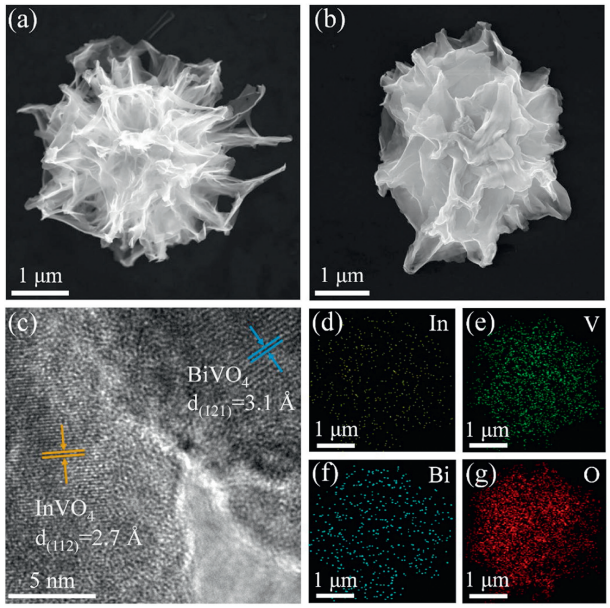


Fig. 1. SEM images of (a) $InVO_4$ and (b) $InVO_4/BiVO_4$. (c) HRTEM image of $InVO_4/BiVO_4$. (d – g) EDS elemental mapping images (In, V, Bi and O) of $InVO_4/BiVO_4$.

Z-scheme heterojunction of $InVO_4/BiVO_4$. Compared to traditional self-assembly method, this approach constructs tighter heterojunction interfaces, thus significantly improving charge transport and separation efficiency, and boosting photocatalytic activity.

The synthesis process for the $InVO_4/BiVO_4$ heterojunction is illustrated in Scheme S1 (Supporting information), and specific steps are described in experimental section in Supporting information. Initially, an $InVO_4$ substrate was prepared using a hydrothermal method [27]. Scanning electron microscopy (SEM), transmission electron microscopy (TEM) and atomic force microscopy (AFM) characterizations revealed that the prepared $InVO_4$ exhibits a nanoflower structure with an average size of approximately 3-4 μm (Fig. 1a and Fig. S1 in Supporting information), which is composed of nanosheets with a thickness of 2–2.5 nm (Figs. S2 and S3 in Supporting information). Subsequently, Bi^{3+} ions were introduced onto the surface of $InVO_4$, and through cation exchange and *in-situ* conversion, the $InVO_4/BiVO_4$ composite material was generated. SEM, TEM and AFM images show that the composite maintains the original nanoflower morphology of the $InVO_4$ substrate (Fig. 1b, Figs. S4 and S5 in Supporting information), indicating that the cation exchange process did not significantly alter its morphology and size. High-resolution TEM (HRTEM) image of $InVO_4/BiVO_4$ displays a lattice spacing of 2.7 Å corresponding to the (112) plane of orthorhombic $InVO_4$ and a lattice spacing of 3.1 Å for the (121) plane of monoclinic $BiVO_4$ (Fig. 1c), initially verifying the successful conversion of $BiVO_4$ onto $InVO_4$. Additionally, energy-dispersive X-ray spectroscopy (EDS) analysis indicated a uniform distribution of In, Bi, O, and V elements in the $InVO_4/BiVO_4$ composite (Figs. 1d–g), suggesting the uniform growth of $BiVO_4$ on $InVO_4$. It is noteworthy that the morphology of $InVO_4/BiVO_4$ heterojunction differs significantly from that of $InVO_4$:$BiVO_4$ composite (prepared *via* traditional electrostatic attraction method, see details in Supporting information), in which $BiVO_4$ large particles are positioned on the side of the $InVO_4$ nanoflower (Fig. S6 in Supporting information). X-ray diffraction (XRD) and Raman spectroscopy measurements further confirmed the presence of both $InVO_4$ and $BiVO_4$ in the composite. As illustrated in Fig. S7 (Supporting information), the characteristic diffraction peaks of pure $InVO_4$ match well with those of orthorhombic $InVO_4$ (JCPDS No. 48–0898). With the introduction of Bi^{3+} ions, the characteristic diffraction peaks at 28.9° and 30.5° of $BiVO_4$ (corresponding to JCPDS No. 14–0688) are clearly observed, and as the amount of Bi^{3+} introduced increased, the diffraction peaks of $BiVO_4$ become more intense. Quantitative analysis of the In and Bi elements within the composite revealed an effective modulation of the conversion ratio of $BiVO_4$, ranging from 2.45 % to 7.99 % (Table S1 in Supporting information). As presented in Fig. S8 (Supporting information), the $InVO_4/BiVO_4$ composite exhibits characteristic peaks at 918 and 826 cm^{-1}, attributed to the V–O–In and V–O–Bi stretching vibrations of $InVO_4$ and $BiVO_4$, respectively [39,40].

X-ray photoelectron spectroscopy (XPS) measurements further confirmed the successful conversion of $BiVO_4$ onto the $InVO_4$ substrate, clearly identifying the characteristic signals of In, Bi, O and V elements (Fig. S9 in Supporting information). Additionally, high-resolution XPS measurements unveiled that the characteristic peaks of In $3d_{5/2}$ and In $3d_{3/2}$ in $InVO_4$ reside at 444.3 and 451.9 eV, respectively, whereas the characteristic peaks of Bi $4f_{7/2}$ and Bi $4f_{5/2}$ in $BiVO_4$ are positioned at 159.7 and 165.0 eV (Fig. S10 in Supporting information). Notably, the binding energies of In 3d and Bi 4f in the $InVO_4/BiVO_4$ composite shifted positively by 0.20 eV and negatively by 0.15 eV, respectively, compared to their individual component values, suggesting strong electronic coupling between $InVO_4$ and $BiVO_4$ (Fig. 2a (left) and Fig. S10). This inference can be further confirmed by theoretical simulations. As presented in Figs. 2b and c, there are significant charge density differences at the $InVO_4/BiVO_4$ heterojunction interface, with charge density decreasing on the $InVO_4$ side and increasing on the $BiVO_4$ side. Bader charge analysis indicated a charge transfer of approximately 2.2 electrons from $InVO_4$ to $BiVO_4$ at the interface.

Ultraviolet-visible diffuse reflectance spectra (UV–vis DRS) measurements revealed that both $InVO_4$ and $BiVO_4$ possess good visible light response, with corresponding band gaps (E_g) of 2.41 and 2.12 eV, respectively (Figs. S11 and S12 in Supporting information). The valence band maximum potentials (E_{VB}) of $InVO_4$ and $BiVO_4$ were determined by ultraviolet photoelectron spectroscopy (UPS) measurements to be 1.54 and 2.22 V, respectively, *versus* the standard hydrogen electrode (*vs.* SHE) (Fig. S13 in Supporting information). Consequently, the conduction band minimum potentials (E_{CB}) for $InVO_4$ and $BiVO_4$ can be calculated as −0.87 and 0.10 V *vs.* SHE, respectively, which are close to the flat-band potential values obtained from Mott–Schottky plots (Fig. S14 in Supporting information). In addition, the work functions of $InVO_4$ and $BiVO_4$ were determined by UPS measurements to be 4.25 and 5.27 eV, respectively. The significant difference in work functions between $InVO_4$ and $BiVO_4$ provides a strong driving force for charge transfer at the $InVO_4/BiVO_4$ heterostructure interface. Specifically, free electrons in $InVO_4$ tend to transfer to $BiVO_4$, leading to the formation of a unified Fermi level. This transfer behavior is consistent with aforementioned XPS analysis and theoretical calculation results. In this equilibrium state, negative charges accumulate on the $BiVO_4$ side and positive charges accumulate on the $InVO_4$ side, resulting in the formation of a built-in electric field pointing from $InVO_4$ to $BiVO_4$. Upon illumination, the electrons in the valence bands (VB) of $BiVO_4$ and $InVO_4$ transition to their respective conduction bands (CB). Due to the presence of the built-in electric field, the photogenerated electrons in the CB of $BiVO_4$ are driven to recombine with photogenerated holes in the VB of $InVO_4$. This process enables the photogenerated electrons in the CB of $InVO_4$ and photogenerated holes in the VB of $BiVO_4$ to remain separated (Fig. 2d).

The above hypotheses regarding the charge transfer mechanism in the $InVO_4/BiVO_4$ heterostructure can be confirmed by *in-situ* illumination XPS (ISI-XPS) and electron spin resonance (ESR) measurements. As shown in Fig. 2a (right) and Fig. S15 (Supporting information), the characteristic peaks of In 3d shifted towards lower

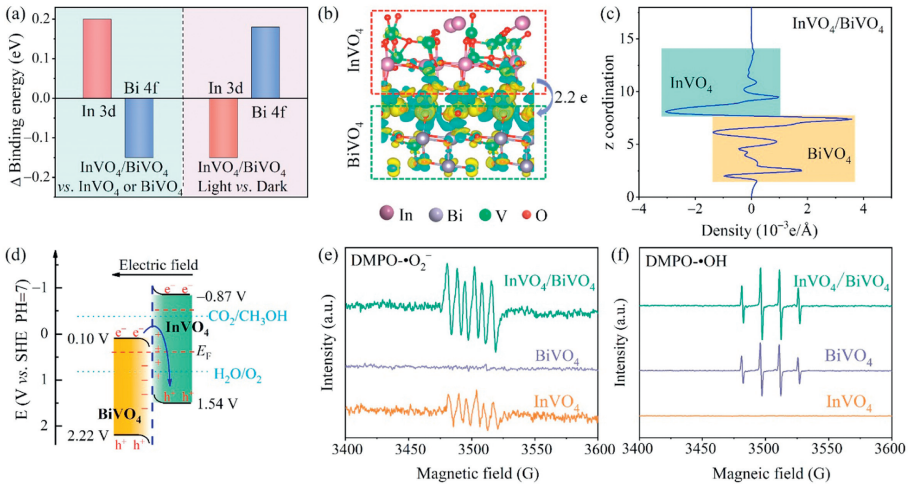


Fig. 2. (a) Binding energy shifts between $InVO_4/BiVO_4$ and $InVO_4$ or $BiVO_4$ in the dark (left), and binding energy shifts of $InVO_4/BiVO_4$ upon light irradiation (light). (b) Charge density difference of the $InVO_4/BiVO_4$ heterojunction. (c) Planar-averaged charge density difference along the *z*-axis. (d) Schematic diagram of the energy band structure and direct Z-scheme charge transfer mechanism under illumination for $InVO_4/BiVO_4$. The EPR spectra of (e) DMPO-$^{\bullet}O_2^-$ and (f) DMPO-$^{\bullet}$OH for $InVO_4$, $BiVO_4$ and $InVO_4/BiVO_4$.

binding energy by 0.15 eV, while the binding energy of Bi 4f shifted towards higher value by 0.18 eV in the $InVO_4/BiVO_4$ under illumination. In contrast, the binding energies of pure $InVO_4$ and $BiVO_4$ remained nearly unchanged under the same conditions (Fig. S16 in Supporting information). These photoinduced shifts in binding energies indicate that photogenerated electrons flow from $BiVO_4$ to $InVO_4$ within the $InVO_4/BiVO_4$ heterostructure, supporting the hypothesis that photogenerated carriers follow a Z-scheme transfer path in the heterostructure. Moreover, the DMPO-$^{\bullet}O_2^-$ signal intensity of $InVO_4/BiVO_4$ is significantly higher than that of $InVO_4$, while the DMPO-$^{\bullet}O_2^-$ signal of $BiVO_4$ is nearly undetectable (Fig. 2e). Simultaneously, the DMPO-$^{\bullet}$OH signal intensity of $InVO_4/BiVO_4$ is also significantly higher than that of $BiVO_4$, while the DMPO-$^{\bullet}$OH signal of $InVO_4$ is barely observable (Fig. 2f). By comparing the redox potentials of $O_2/^{\bullet}O_2^-$ (−0.33 V *vs.* SHE) and $H_2O/^{\bullet}$OH (1.99 V *vs.* SHE), if the charge transfer mechanism of the $InVO_4/BiVO_4$ heterostructure is the traditional type-II double charge transfer, $^{\bullet}$OH and $^{\bullet}O_2^-$ radicals should not be produced. However, the experimental results contradicted this assumption, further confirming the formation of a Z-scheme charge transfer pathway, which effectively retained photogenerated electrons in the CB of $InVO_4$ and photogenerated holes in the VB of $BiVO_4$, achieving efficient carrier separation. To further investigate the improved charge separation efficiency in the $InVO_4/BiVO_4$ heterostructure, electrochemical impedance spectroscopy (EIS) and transient photocurrent measurements were conducted. Figs. S17 and S18 (Supporting information) demonstrate that, compared to $InVO_4$, $BiVO_4$ and $InVO_4$:$BiVO_4$, $InVO_4/BiVO_4$ exhibits the smallest charge transfer resistance (Table S2 in Supporting information) and the largest photocurrent density. These results indicate that the tightly connected heterostructure formed through the ion-exchange and *in-situ* partial conversion strategy can significantly accelerate charge carrier migration and separation capabilities.

Gas chromatography analysis revealed that the main photocatalytic CO_2 reduction products for these $InVO_4$-based materials were CH_3OH, accompanied by a small amount of CO, while pure $BiVO_4$ exhibits negligible photocatalytic CO_2 reduction activity due to thermodynamic limitation of reduction. As summarized in Fig. 3a, pristine $InVO_4$ displays a moderate activity with a CH_3OH yield of 58.1 μmol g^{-1} h^{-1}. The $InVO_4$:$BiVO_4$ achieves a slight increase in the performance with a CH_3OH yield of 65.0 μmol g^{-1} h^{-1}, indicating that the simple electrostatic self-assembly does not effectively enhance carrier separation. In contrast, $InVO_4/BiVO_4$

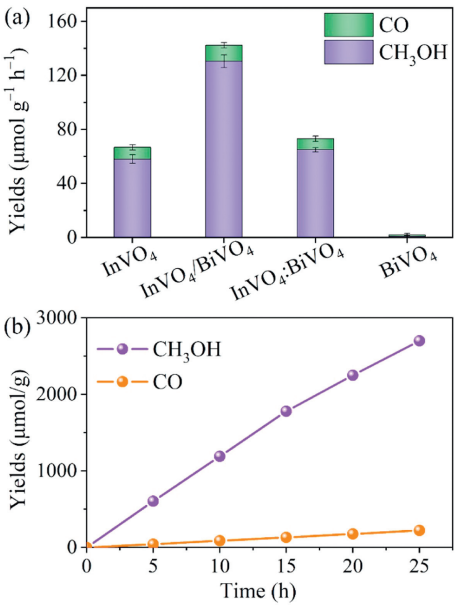


Fig. 3. (a) Yields of products with different photocatalysts. (b) Time-on-line amounts of products by $InVO_4/BiVO_4$.

demonstrates a significant improvement in photocatalytic activity (Fig. S19 in Supporting information), and the optimized yield of CH_3OH reaches 130.5 μmol g^{-1} h^{-1} with a high selectivity of 92 %, which is 2.2 and 2.0 times higher than that of pure $InVO_4$ and $InVO_4$:$BiVO_4$, respectively, and superior to those of semiconductor photocatalysts reported under similar conditions (Table S3 in Supporting information). Additionally, the O_2 yield of $InVO_4/BiVO_4$ is 221.2 μmol g^{-1} h^{-1}, indicating a balanced consumption of photogenerated electrons and holes (Fig. S20 in Supporting information).

The $InVO_4/BiVO_4$ heterostructure also demonstrates excellent photoreaction stability. Fig. 3b and Fig. S21 (Supporting information) illustrate that it maintained high catalytic activity throughout a continuous 25 h illumination reaction and displayed no significant decrease in activity after 4 cycles of reaction tests. The crystal structure and surface state of $InVO_4/BiVO_4$ remained stable during the reaction process, as confirmed by XRD patterns and

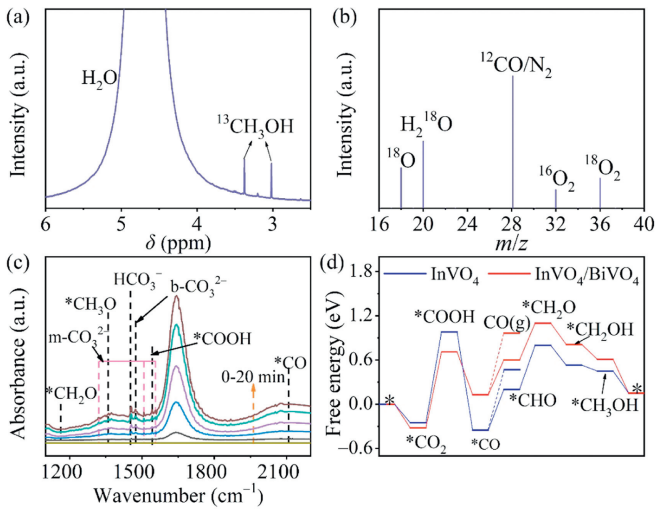


Fig. 4. (a) ^{1}H NMR spectrum of the products produced from $^{13}CO_2$ reduction. (b) MS analyses for solar-driven reaction of $H_2{}^{18}O$ to $^{18}O_2$ ($m/z = 36$) using $InVO_4/BiVO_4$ as photocatalyst. (c) IS-IR spectra of the CO_2 photoreduction reaction with $InVO_4/BiVO_4$ as photocatalyst. (d) Calculated free-energy plots for CO_2 photoreduction of $InVO_4$, and $InVO_4/BiVO_4$.

XPS spectra (Figs. S22 and S23 in Supporting information). Moreover, control experiments revealed that light, catalyst, CO_2, and H_2O are indispensable elements for the generation of CH_3OH, indicating that CH_3OH originates from light-driven CO_2 reduction over photocatalyst with water as electron source (Fig. S24 in Supporting information). Furthermore, when $^{13}CO_2$ was employed as the reactant, distinctive split peaks attributable to $^{13}CH_3OH$ ($\delta = 3.04$ and 3.40 ppm) were discernible in the ^{1}H nuclear magnetic resonance spectrum (Fig. 4a). Meanwhile, the replacement of $H_2{}^{16}O$ with $H_2{}^{18}O$ resulted in unequivocal detection of $^{18}O_2$ ($m/z = 36$) through mass spectrometry analysis (Fig. 4b). These results further robustly demonstrated that CH_3OH and O_2 originate from CO_2 photoreduction and H_2O oxidation, respectively.

In-situ infrared spectroscopy (IS-IR) measurements were carried out to monitor the evolution of CO_2 on the $InVO_4/BiVO_4$ surface during photocatalytic reaction. As shown in Fig. 4c, the characteristic absorption peaks emerged for various intermediates like m-$CO_3{}^{2-}$ (1321, 1508 and 1556 cm^{-1}), b-$CO_3{}^{2-}$ (1476 cm^{-1}), $HCO_3{}^{-}$ (1454 cm^{-1}) and *COOH (1542 cm^{-1}) [41–43], with increasing illumination time. Additionally, the characteristic signal peaks of *CH_2O (1163 cm^{-1}) and *CH_3O (1362 cm^{-1}) [44,45], which are crucial intermediates in the reduction of CO_2 to CH_3OH, were also identified. Based on these observations, the reaction pathway for photocatalytic CO_2 reduction on the $InVO_4/BiVO_4$ heterojunction surface can be speculated as follows. Photoexcited $InVO_4/BiVO_4$ generates electron-hole pairs separated *via* a Z-scheme mechanism, retaining electrons on $InVO_4$ and holes on $BiVO_4$. Electrons on $InVO_4$ drive CO_2 reduction through proton-coupled electron transfer, forming *CO *via* *COOH protonation and dehydration, followed by consecutive reduction and hydrogenation to CH_3OH. Furthermore, density functional theory (DFT) calculations determined the Gibbs free energies of the reaction intermediates. As illustrated in Fig. 4d, CO_2 adsorbed at the reduction site was first activated to form *CO_2, and the adsorption effect of $InVO_4/BiVO_4$ on CO_2 is more significant than that of $InVO_4$, mainly attributed to the transfer of free electrons in $InVO_4/BiVO_4$, rendering $InVO_4$ in an electron-deficient state. The rate-determining step for both $InVO_4$ and $InVO_4/BiVO_4$ is the transition from *CO_2 to *COOH, but with a significantly lower energy barrier for $InVO_4/BiVO_4$ than that of $InVO_4$. Subsequently, *COOH undergoes protonation and dehydration to form a stable *CO intermediate. Notably, hydrogenation of *CO to *CHO has a lower energy barrier than *CO desorption, contributing to high selectivity of $InVO_4$-based materials in reducing CO_2 to CH_3OH.

In summary, a Z-scheme heterojunction of $InVO_4/BiVO_4$ was successfully synthesized through an innovative cation exchange strategy and utilized for photocatalytic CO_2 reduction with H_2O as the electron source. Microstructural analysis unveiled that the $InVO_4/BiVO_4$ features a tightly connected interface, enabling efficient separation of photogenerated carrier through a Z-scheme mechanism, as validated by diverse measurements encompassing ESR, ISI-XPS and photoelectrochemical techniques. Furthermore, DFT calculations revealed that the formation of heterojunction can promote the adsorption and activation of CO_2, attributed to the deficient-electron nature of the $InVO_4$ component. Consequently, the $InVO_4/BiVO_4$ heterojunction demonstrates remarkable efficiency and selectivity in photocatalytic CO_2 reduction to CH_3OH, achieving a yield and selectivity of 130.5 μmol g^{-1} h^{-1} and 92 % respectively, outperforming other materials reported thus far.

Declaration of competing interest

The authors declare that they have no known competing financial interests or personal relationships that could have appeared to influence the work reported in this paper.

CRediT authorship contribution statement

Cheng-Cheng Jiao: Writing – original draft, Methodology, Investigation. **Guang-Xing Dong:** Writing – original draft, Methodology, Investigation. **Ke Su:** Writing – review & editing, Supervision, Project administration, Methodology. **You-Xiang Feng:** Investigation. **Min Zhang:** Writing – review & editing, Supervision, Project administration, Methodology, Funding acquisition, Conceptualization. **Tong-Bu Lu:** Methodology, Funding acquisition.

Acknowledgments

This work was financially supported the National Key R&D Program of China (No. 2022YFA1502902), the National Natural Science Foundation of China (NSFC, Nos. 22475152 and U21A20286), and the 111 Project of China (No. D17003).

Supplementary materials

Supplementary material associated with this article can be found, in the online version, at doi:10.1016/j.cclet.2024.110752.

References

[1] S. Fang, M. Rahaman, J. Bharti, et al., Nat. Rev. Methods Prim. 3 (2023) 61.
[2] S. Yang, W.J. Byun, F. Zhao, et al., Adv. Mater. 36 (2024) 2312616.
[3] T. Wang, Y. Wang, Y. Li, C. Li, Nano Res. 17 (2024) 5–17.
[4] Y. Li, Y. Wei, W. He, et al., Chin. Chem. Lett. 34 (2023) 108417.
[5] Q. Tang, T. Li, W. Tu, et al., Adv. Funct. Mater. 34 (2024) 2311609.
[6] C. Liu, F. Chen, B.H. Zhao, Y. Wu, B. Zhang, Nat. Rev. Chem. 8 (2024) 277–293.
[7] B. Su, Y. Kong, S. Wang, et al., J. Am. Chem. Soc. 145 (2023) 27415–27423.
[8] W.J. Wang, K. Chen, Chin. Chem. Lett. 36 (2025) 109998.
[9] S.X. Yuan, K. Su, Y.X. Feng, et al., Chin. Chem. Lett. 34 (2023) 107682.
[10] H.K. Wang, M.R. Zhang, K. Su, et al., Sci. China Mater. 67 (2024) 3176–3184.
[11] X. Deng, Y. Ke, J. Ding, et al., Chin. Chem. Lett. 35 (2024) 109064.
[12] Z. Xie, H. Luo, S. Xu, L. Li, W. Shi, Adv. Funct. Mater. 34 (2024) 2313886.
[13] Z. Ye, K.R. Yang, B. Zhang, et al., Proc. Natl. Acad. Sci. U. S. A. 121 (2024) e2408183121.
[14] J. Wu, F. Huang, Q. Hu, et al., J. Am. Chem. Soc. 146 (2024) 26478–26484.
[15] H. Jian, K. Deng, T. Wang, et al., Chin. Chem. Lett. 35 (2024) 108651.
[16] B. Shang, F. Zhao, S. Suo, et al., J. Am. Chem. Soc. 146 (2024) 2267–2274.
[17] H. Lu, N. Uddin, Z. Sun, et al., Nano Energy 115 (2023) 108684.
[18] M. Cheng, N. Cao, Z. Wang, et al., ACS Nano 18 (2024) 10582–10595.
[19] Q. Sun, X. Liu, Q. Gu, et al., J. Am. Chem. Soc. 146 (2024) 28885–28894.
[20] C.L. Rooney, M. Lyons, Y. Wu, et al., Angew. Chem. Int. Ed. 63 (2024) e202310623.

[21] Y. Wang, R. Godin, J.R. Durrant, J. Tang, Angew. Chem. Int. Ed. 60 (2021) 20811–20816.
[22] Z. Shang, X. Feng, G. Chen, R. Qin, Y. Han, Small 19 (2023) 2304975.
[23] C. Shen, X.Y. Meng, R. Zou, et al., Angew. Chem. Int. Ed. 63 (2024) e202402369.
[24] J.R. Huang, W.X. Shi, S.Y. Xu, Adv. Mater. 36 (2024) 2306906.
[25] L. Wang, B. Zhu, J. Zhang, et al., Matter 5 (2022) 4187–4211.
[26] H. Chen, X. Yang, M. Lin, et al., ACS Sustain. Chem. Eng. 11 (2023) 18029–18040.
[27] Q. Han, X. Bai, Z. Man, et al., J. Am. Chem. Soc. 141 (2019) 4209–4213.
[28] M.Y. Ye, Z.H. Zhao, Z.F. Hu, et al., Angew. Chem. Int. Ed. 56 (2017) 8407–8411.
[29] Y. Liu, H. Shang, B. Zhang, D. Yan, X. Xiang, Nat. Commun. 15 (2024) 8155.
[30] J. Li, F. Wei, Z. Xiu, X. Han, Chem. Eng. J. 446 (2022) 137129.
[31] M. Yu, J. Wang, G. Li, S. Zhang, Q. Zhong, J. Mater. Sci. Technol. 154 (2023) 129–139.
[32] D.S. Lee, Y.W. Chen, J. CO_2 Util. 10 (2015) 1–6.
[33] G.X. Dong, M.R. Zhang, Su K, et al., J. Mater. Chem. A 11 (2023) 9989–9999.
[34] J. Xu, Z. Bai, X. Xin, A. Chen, H Wang, Chem. Eng. J. 337 (2018) 684–696.
[35] J.B. Pan, B.H. Wang, S. Shen, L. Chen, S.F. Yin, Angew. Chem. Int. Ed. 62 (2023) e202307246.
[36] F. Guo, W. Shi, X. Lin, et al., Sep. Purif. Technol. 141 (2015) 246–255.
[37] Y. Fan, R. Yang, R. Zhu, Colloid Surf. A 589 (2020) 124448.
[38] L. Yu, H. Wang, Q. Huang, et al., Sep. Purif. Technol. 310 (2023) 123143.
[39] W. Sun, Y. Dong, X. Zhai, et al., Chem. Eng. J. 430 (2022) 132872.
[40] D. Ma, Y. Zhang, M. Gao, et al., Appl. Surf. Sci. 353 (2015) 118–126.
[41] C. Chen, C. Ye, X. Zhao, et al., Nat. Commun. 15 (2024) 7825.
[42] K. Wang, M. Cheng, F. Xia, et al., Small 19 (2023) 2207581.
[43] P. Liu, Y.L. Men, X.Y. Meng, et al., Angew. Chem. Int. Ed. 62 (2023) e202309443.
[44] X. Duan, H. Jia, T. Cao, et al., Appl. Catal. B 352 (2024) 124016.
[45] Z. Wang, J. Zhu, X. Zu, et al., Angew. Chem. Int. Ed. 61 (2022) e202203249.